ARTICLE   OPEN

Check for updates

Imaging the effect of high photoexcited densities on valley polarization and coherence in MoS$_2$ monolayers

F. Cadiz [1 ✉], S. Gerl [1], T. Taniguchi [2] and K. Watanabe [3]

We have investigated the laser-induced valley polarization and coherence of encapsulated MoS$_2$ monolayer as a function of temperature, power density, and spatial position. Besides a non-monotonic dependence on temperature, recently attributed to a dependence of the valley relaxation time on the momentum scattering rate, we observe a two-fold increase of the valley polarization when increasing the laser excitation power. We attribute this effect to a local heating induced by the energy relaxation of photoexcited excitons and to an increase of the exciton-exciton scattering rate. In contrast, only a moderate enhancement of valley coherence is observed, which exhibits a dramatic drop after further increasing the excitation power. We attribute this behaviour to the detrimental role of exciton-exciton interactions on the pure dephasing rate responsible for the loss of coherence between the valleys. This manifests itself by a strong dip in the spatial profile of the valley coherence at high photoexcited densities.

INTRODUCTION

Atomically thin layers of transition metal dichalcogenides (TMD) such as MX_2 (M = Mo, W; X = S, Se, Te) have emerged as promising 2D semiconductors for applications in valley/spintronics[1–3]. In monolayers, the interplay between inversion symmetry breaking and the strong spin-orbit interaction inherent to the heavy transition metal atoms yields a spin/valley texture at the K^+/K^- points of the Brillouin zone, which is expected to provide additional functionalities in future devices[2,4–6]. Due to enhanced Coulomb interaction in 2D, weak dielectric screening and large effective masses, the optical excitation couples mostly to exciton resonances[7–9]. Remarkably, light absorption due to these strongly bound excitons preserves the single-particle coupling between light chirality and the valley degree of freedom[10–14]. Moreover, the short exciton lifetime at cryogenic temperatures[15] is comparable to the dephasing time[16], so that coherent superpositions of K^+ and K^- valley excitons can be detected in simple steady-state photoluminescence (PL) experiments[17–19]. However, there is still a lack of understanding of the different microscopic mechanisms that govern valley polarization and coherence in TMD monolayers. In this work, we have fabricated encapsulated monolayer MoS$_2$ heterostructures; and we present an investigation of the spatially resolved, steady-state valley polarization and coherence of neutral excitons as a function of sample temperature and excitation power density. At low excitation power, we find that both valley polarization and coherence attain a local maximum at a temperature of 40 ± 3 K, in agreement with very recent observations[20]. We show that, at a fixed temperature of $T = 6$ K, a similar enhancement of the valley polarization can be achieved by increasing the laser power density. The valley polarization attains a maximum at a photoexcited density of $n^* \sim 5 \times 10^{10}$ cm^{-2}, and slowly decreases for densities above n^*. We attribute this to two laser-related effects: local heating and increased rate of exciton-exciton scattering events. The latter is particularly detrimental to valley coherence, for which we see only a small enhancement at

n^*, and a dramatic decrease upon further increase of the excitation power. Spatially resolved PL shows that valley coherence develops a significant spatial gradient at high densities, reflecting the important role of the exciton density on the dynamics of valley coherence.

RESULTS AND DISCUSSION

Sample characterization

Fig. 1 a shows a schematic drawing of the MoS$_2$-based Van der Waals heterostructure deposited onto a SiO$_2$/Si substrate. A thin graphite flake is used to screen possible charge puddles located on the SiO$_2$ substrate[21] and also to minimize reflections of the PL coming from the substrate, which could affect PL imaging. A microscope image of the sample under white light illumination is shown in Fig. 1b. The high-optical quality of our sample is confirmed by a ~2 meV neutral exciton linewith in PL at low temperatures and low excitation power, close to the homogeneous limit[16,19,22].

Figure 1 c shows the spatially averaged PL spectrum, decomposed into its co-polarized (I_{co}) and cross-polarized (I_{cross}) components with respect to the laser polarization for a low excitation power of 20μW. Also shown is the degree of polarization at each emitted photon energy, defined as $\mathcal{P} = (I_{co} - I_{cross})/(I_{co} + I_{cross})$. Under circular excitation, excitons are selectively generated in either the K^+ or the K^- valley depending on the laser's helicity. The steady-state degree of circular polarization of the PL, given by $\mathcal{P}_C = \tau_v/\tau$, reflects the ratio between the valley lifetime τ_v and the exciton lifetime τ. Under linear excitation, a coherent superposition of excitons in the K^+ and K^- valleys is generated[17]. The phase coherence between the valleys in the superposition is lost after the valley coherence time τ_{vc} given by $1/\tau_{vc} = 1/(2\tau_v) + \gamma_v^*$, where γ_v^* is the pure (valley) dephasing rate. Due to the very short exciton lifetime τ in the picosecond (ps) range[15,23–26], comparable to the valley
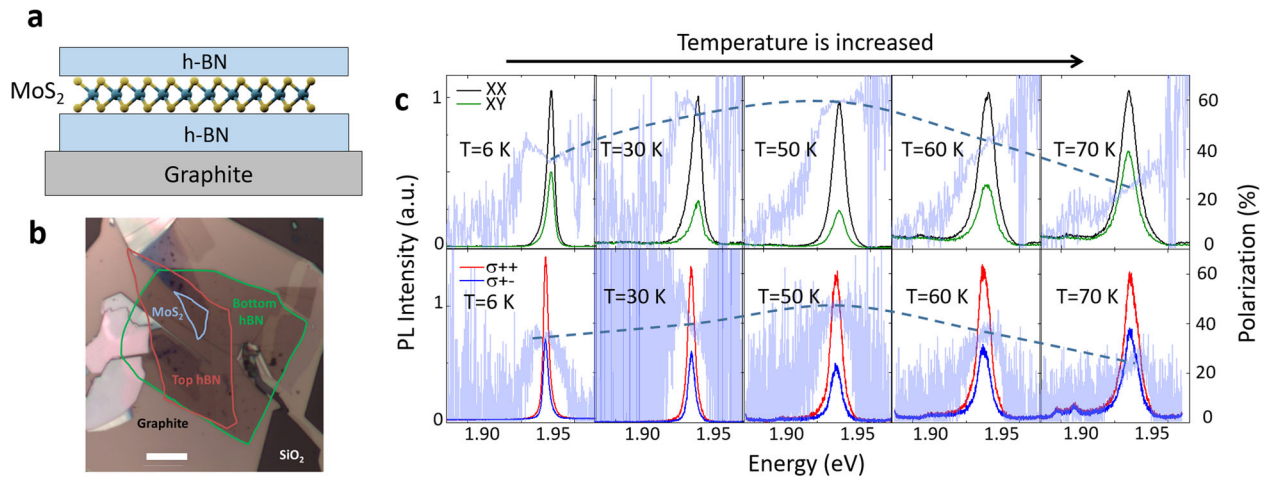
Fig. 1 Temperature dependence of valley polarization and coherence of monolayer MoS$_2$. a Schematic side-view of the sample. The MoS$_2$ monolayer is encapsulated between two thin h-BN flakes to provide high-optical quality and to prevent photodoping effects. A thin graphite flake is used to screen charge disorder from the substrate and to avoid back reflections for PL imaging. The whole heterostructure is deposited onto a silicon substrate with a 90 nm-thick silicon dioxide layer. **b** Microscope image of the sample. The length of the scale bar is 10 μm. **c** Polarization-resolved PL spectra under linear (top) and circular (bottom) excitation at 1.96 eV for different sample temperatures. The excitation power was kept at 20 μW. Also shown is the degree of polarization as a function of photon emission energy. The dashed lines are a guide to the eye indicating the polarization at the energy at which the PL intensity is maximum.

coherence time τ_{vc}, this valley superposition is partially preserved before radiative recombination yielding a degree of linear polarization $\mathcal{P}_L = \tau_{vc}/\tau$ of the PL. The observation $\mathcal{P}_L > \mathcal{P}_C$ allows one to conclude that, at these low photoexcitation densities, the valley coherence time is mostly limited by τ_v.

Temperature dependence of valley polarization and coherence

Remarkably, increasing the sample temperature leads to an increase of both the valley polarization $\mathcal{P}_C$ and the valley coherence $\mathcal{P}_L$, both peaking at $T \sim 40$ K, before decreasing again upon further increase of the temperature. This is in agreement with very recent findings[20]. At $T \sim 40$ K the degree of valley polarization can reach $\mathcal{P}_C \sim 50\%$, whereas valley coherence can be as high as $\mathcal{P}_L \sim 60\%$ although this maximum value was found to be sample and position-dependent, probably due to inhomogeneities of the dielectric environment and strain.

These findings can be ascribed to a non-monotonic temperature dependence of the valley lifetime τ_v that can be explained by the competition of two mechanisms, as discussed by Wu et al.[20]. At low temperatures the valley lifetime is limited by the long-range electron-hole exchange interaction, in the so-called Maialle–Silva–Sham (MSS) mechanism[23,27]. This interaction is equivalent to an effective magnetic field around which the valley pseudospin precesses with a Larmor frequency $\Omega(\vec{k})$, where $\vec{k}$ is the exciton's center-of-mass momentum. This is similar to the Dyakonov-Perel spin-relaxation mechanism in non-centrosymmetric semiconductors[28]. When the momentum relaxation time τ_c is much shorter than the pseudospin precession time Ω^{-1}, the valley relaxation time varies as $1/(\Omega^2(\vec{k})\tau_c)$. Hence, thermally activated momentum scattering (which shortens τ_c) suppresses the valley pseudospin relaxation. Increasing the temperature will thus be accompanied by an increase of the valley relaxation time τ_v. However, at sufficiently high temperatures the valley lifetime will no longer be limited by the MMS mechanism. Instead, it will be governed by an ultrafast intervalley relaxation driven by phonon mediated processes, which become faster than 1 ps above 100 K[29]. This is likely the reason why the valley lifetime and coherence drop when increasing the temperature above $T \sim 40$ K in our experiments. Under a tightly focused laser excitation, we can therefore expect the valley dynamics to be

strongly power and spatially dependent, which is why we will now focus on PL imaging at different photoexcited exciton densities.

Figure 2 a shows the resulting image of the exciton luminescence at $T = 6$ K and $5 \mu W$ excitation power. The PL spatial distribution exhibits a clear rotational symmetry, so that the PL intensity depends only on the distance r with respect to the laser spot. A radial profile of the PL is obtained by averaging cuts along different directions, the result for Fig. 2a is shown in Fig. 2b for both circular and linear excitation (blue squares and open circles, respectively).

Also shown is the normalized radial profile of the laser (black open circles), and its Gaussian fit (dashed line). Since the PL clearly extends beyond the laser spot, we can obtain an effective diffusion length L by fitting the PL intensity I with the convoluted solution of the steady-state diffusion equation in 2D:

$$I(r) \propto \int_{-\infty}^{+\infty} K_0(|r|/L) e^{-(r-r')^2/\sigma^2} dr' \qquad (1)$$

where K_0 is the modified Bessel function of the second kind and $\sigma = 0.3 \mu m$. This fit is shown by a red line in Fig. 2b and yields a diffusion length of $L = 0.55 \pm 0.025 \mu m$ at $T = 6$ K. Such a large diffusion length is unlikely to reflect the diffusion of bright excitons. Indeed, considering a population decay time of $\tau \sim 5$ ps[15], an exciton mass of $m_X \sim m_0$, where m_0 is the electron mass, a temperature of $T = 10$ K and a momentum relaxation time of $\tau_c = 0.05 - 1$ ps[20], we expect an exciton diffusion length in the range

$$L_X = \sqrt{\frac{k_B T \tau_c}{m_X}} \tau \approx 6 - 28 \text{ nm} \qquad (2)$$

where k_B is Boltzmann's constant (here we have assumed that Einstein's relation is valid even for such a short-lived species). This is at least 18 times smaller than the observed effective diffusion length of $L \approx 0.5 \mu m$ at $T = 6$ K. Moreover, it has been predicted that exciton transport should be anisotropic under linear excitation[30], but as shown in Fig. 2b, no difference is observed in the spatial profiles between circular and linear excitation. Recently, it has been shown in encapsulated MoSe$_2$ monolayers that the PL intensity at cryogenic temperatures displays a spatial profile that extends over 1.5 μm, for both neutral excitons and trions despite their very different (and short) lifetimes. It has been proposed that the observed PL spatial distribution at low
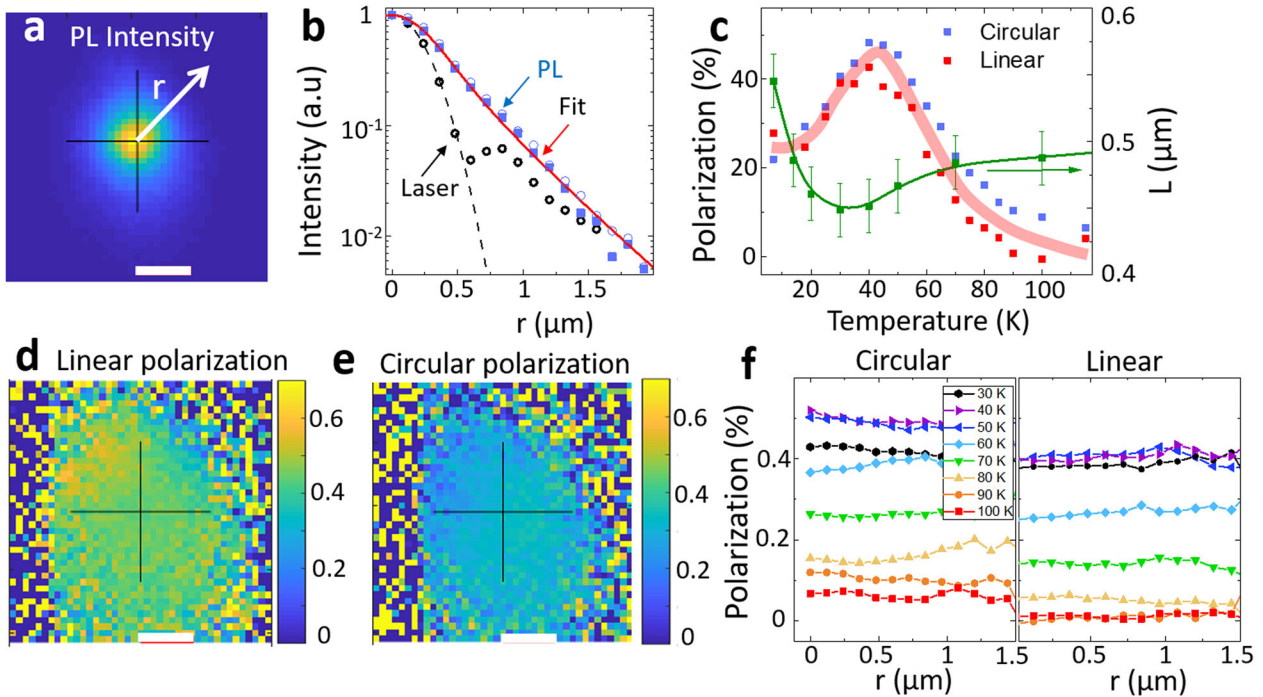
Fig. 2 Imaging the spatial distribution of excitons and their valley index. a Spatially resolved PL intensity under cw laser excitation at 5 μW at T=6 K. The radial distance with respect to the excitation spot is denoted by r. The length of the scale bar is 1 μm. **b** Radial profile of the PL intensity shown in (**a**) obtained after averaging over different directions, for a circular (squares) and linear (open circles) laser excitation. Also shown is the laser profile (black circles) together with a Gaussian profile (dashed black line) with a radius of 0.3 μm. The red line is a fit with a solution of the 2D diffusion equation (Eq. (1)) giving an effective diffusion length of $L = 0.55 \pm 0.025$ μm. **c** Degree of polarization under circular and linear excitation for an excitation power of 20 μW as a function of sample temperature. Also shown is the effective diffusion length L extracted from the spatially resolved PL images. Continuous lines are a guide to the eye. **d** Spatially resolved linear polarization under linear excitation for the same conditions as (**a**). Same scale as in (**a**). **e** Spatially resolved circular polarization under circular excitation for the same conditions as (**a**). Same scale as in (**a**). **f** Radial profile of the photoluminescence's circular and linear polarization for selected values of the sample temperature. The laser excitation is kept at 20 μW.

temperatures is likely to be the result of fast hot-exciton propagation which occurs before relaxing into the light-cone[31]. Indeed, the diffusion length of hot excitons can be orders of magnitude larger than that of bright excitons due to their much larger effective temperature[32] and because the relaxation time into the light-cone can be larger than the exciton radiative lifetime at cryogenic temperatures[33]. Varying the sample temperature produces a slight change in the measured effective diffusion length L, as shown in Fig. 2c together with the degree of valley polarization and valley coherence. It is found that L decreases from 0.55 μm at $T = 6$ K down to 0.45 μm at $T = 30$ K. An increase of the scattering rate with temperature is indeed consistent with a reduced distance over which hot excitons can travel before energy relaxation. This simple picture explains why, when the temperature is increased, L decreases while the valley polarization and coherence increase. The non-monotonic behavior of L with temperature could be due to the competition between a shortening of the momentum relaxation time and the increase of diffusivity with temperature.

Another key result which is consistent with our interpretation of the PL profiles is the spatial dependence of the degree of circular (or linear) polarization of the PL. As shown in Fig. 2d, e, the polarization is approximately constant in space at low excitation power at $T = 6$ K. In our scenario, a spatially constant polarization is consistent with the fact that the PL spot reflects the initial bright exciton distribution and not bright exciton diffusion. One alternative explanation would be that both the valley polarization and the valley coherence lifetimes are much longer than the exciton lifetime τ, so that no loss of polarization occurs during exciton propagation. If this was the case, however, we should observe a close to 100 %-polarized emission at low temperatures

and one should be able to observe a spatial decay of the polarization at sufficiently high temperature. Figure 2f shows that changing the sample temperature up to $T = 100$ K only changes the overall degree of polarization, but it remains spatially independent at all temperatures.

The role of exciton-exciton interactions

Wu and co-workers[20] have shown that the enhancement of valley polarization can also be achieved by keeping a fixed temperature and adding carriers to the system with the application of a gate bias. This was shown to be detrimental for valley coherence, however, due to an intervalley polaron dressing which results in a higher scattering rate for the in-plane pseudospin. We study another mechanism of valley polarization enhancement: increasing the excitation laser power and, therefore, exciton-exciton interactions. Figure 3a shows the total PL intensity as a function of the excitation power, in a large range going from 1 μW up to 10 mW. Importantly, no change in the PL spectrum is observed after laser exposure at such high power densities, which permits us to exclude the presence of laser-induced photodoping effects[34] thanks to h-BN encapsulation. The linear regime, represented by the red line in Fig. 3a, is valid below 100 μW. Increasing the power leads to a sub-linear behaviour of the exciton luminescence. At 100 μW, we can roughly estimate the photogenerated exciton density to be $n_0 \sim 2 \times 10^9$ cm^{-2} by taking an absorption coefficient of $\alpha = 1$ %, a lifetime $\tau = 5$ ps and a uniform distribution inside a circle of radius $L = 0.5$ μm. We conclude that attributing this non-linearity to the onset of Auger-like exciton-exciton recombination would imply an extremely large Auger coefficient of $\gamma \sim 1/(n_0\tau) = 100$ cm^2 s^{-1}. In addition, the behaviour observed in Fig. 3a cannot
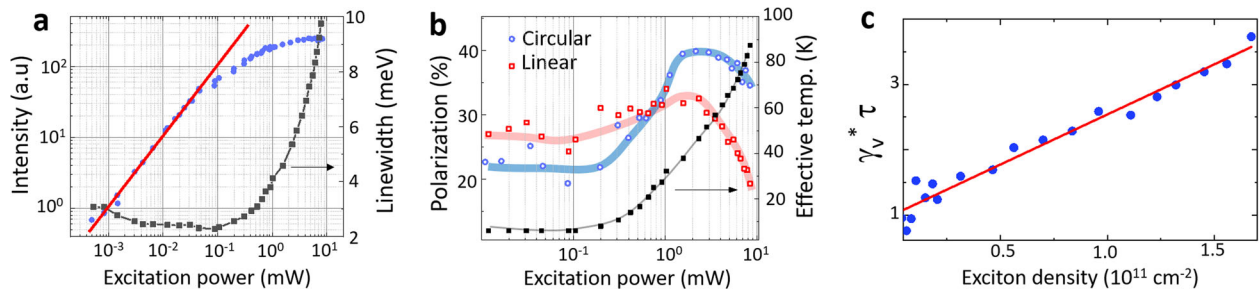
Fig. 3 Spatially averaged valley polarization and coherence at high excitation densities. $T = 6$ K. **a** Integrated PL intensity (blue dots) as a function of the laser excitation power. The red line represents a linear relationship between intensity and excitation power. The exciton linewidth is shown in black squares. **b** Degree of polarization as a function of the laser excitation power. Also shown is the effective temperature extracted from the linewidth of the neutral exciton peak. The continuous lines are a guide to the eye. **c** Extracted $\gamma_v^* \tau$ product as a function of the exciton density, where τ is the exciton lifetime and γ_v^* the pure dephasing rate of valley coherence.

be described by a simple model based solely on exciton-exciton annihilation since the latter predicts, at high densities, a variation of the intensity I of the form $I \propto \sqrt{P_{ex}}$ where P_{ex} is the excitation power, which does not fit the data. Instead, we attribute the sub-linear behaviour of the PL intensity to a local heating of the lattice created by the relaxation of hot excitons[31]. At 10 mW, the linewidth increases up to 10 meV (Fig. 3a) and the exciton peak redshifts by 5 meV, both consistent with a significant increase of the local temperature up to $T_L \approx 100$ K according to the temperature dependence of the PL spectrum at low excitation power (see Supplementary Notes 1 and 2). This indicates that sources of line broadening other than exciton-phonon interactions do not seem to play a significant role. The PL yield of MoS$_2$ monolayer is reduced by almost one order of magnitude between 6 K and 100 K (see Supplementary Note 1) and this can significantly contribute to the sub-linear behaviour of the photoluminescence.

Since in this temperature range the linewidth is much more sensitive to the temperature than the PL emission energy, we have extracted the effective local temperature induced by the laser excitation by comparing the power-induced broadening of the exciton linewidth with the temperature-induced broadening (shown in the Supplementary Note 1). The result is shown in Fig. 3b, together with the degree of valley polarization $\mathcal{P}_C$ and valley coherence $\mathcal{P}_L$ as a function of excitation power. We note that 100 µW also corresponds to the onset of a rapid increase of the valley polarization, with a two-fold increase from 20 % at low excitation power up to 40 % achieved at 1.5 mW. In this power range, the effective local temperature starts to increase and reaches $T_L = 40$ K. This behaviour is remarkably consistent with the temperature dependence of the valley polarization, confirming that local laser-induced heating is probably at the origin of the observed enhancement. Above $T_L = 40$ K, valley polarization stops to increase and eventually decreases again, but slightly and slowly. This is different, however, to what is expected based solely on temperature effects, which should lead to a sharp polarization drop above $T_L = 40$ K. This can be explained as follows: in addition to the increase of the local temperature, increasing the laser power also modifies the rate of exciton-exciton collisions, which shortens even further the momentum relaxation time τ_c, similar to what has been observed in GaAs[35] where the scattering rate increases linearly with the photoexcited electron density and results in an increase of the spin lifetime. This compensates for the thermal activation of valley relaxation mechanisms other than the MMS mechanism. As a result of the competition between these mechanisms, the valley lifetime τ_v varies weakly above 1 mW. Eventually, exciton-exciton interactions will negatively impact the valley lifetime and so τ_v starts to decrease[36].

Note that, in contrast, valley coherence shows a significantly reduced enhancement effect between 100 µW and 1.5 mW, and rapidly decreases upon further increase of the excitation power.

The reduced enhancement is probably due to the competition between an increase of the valley relaxation time τ_v and an increase of the valley dephasing rate γ_v^* induced by exciton--exciton interactions, which are expected to be significant at photoexcitation densities comparable to $n^* \sim 10^{10}$ cm^{-2}[36]. Indeed, the typical distance between excitons in the $n = 10^{10} - 10^{11}$ cm^{-2} density range is of the order of $\ell \sim 1/\sqrt{\pi n} = 18 - 56$ nm, which seems to compare well with the estimated bright exciton diffusion length. This exciton-exciton interaction is expected to cause similar detrimental effects on valley coherence as, for example, additional charge carriers as recently observed[20]. Since we observe that the valley lifetime τ_v varies weakly at high excitation densities above 1 mW, the rapid decrease in valley coherence can be explained by a significantly increase of the pure dephasing rate γ_v^* that becomes the limiting mechanism that breaks phase coherence between the K^+ and K^- valleys. For a more quantitative analysis of the effect of the photoexcited exciton density n on the valley dephasing rate γ_v^*, we plot in Fig. 3c the quantity $(\mathcal{P}_C/\mathcal{P}_L - 1/2)/\mathcal{P}_C = \tau \gamma_v^*$ as a function of the estimated photo-excited exciton concentration n. We observe a linear relationship between $\tau \gamma_v^*$ and n, the red line is a fit given by $\tau \gamma_v^* = 1.0 + 1.5 \, n(10^{11} \text{cm}^{-2})$. Taking an exciton lifetime of typically $\tau = 5$ ps yields therefore

$$\gamma_v^*(n) = 0.2 + 0.3 \, n(10^{11} \text{cm}^{-2}) \text{ ps}^{-1}. \qquad (3)$$

Spatial profiles at high exciton densities

We finally focus on the spatial evolution of the valley polarization and coherence when increasing the laser power. The normalized radial profiles of the exciton luminescence for selected excitation powers are shown in Fig. 4a. They reveal a moderate broadening of the exciton distribution, probably due to a spatially dependent momentum relaxation time and PL yield which flattens the radial profiles near $r = 0$. It can also be the beginning of the formation of a halo-like profile due to Seebeck drift under the presence of a temperature gradient[31,37,38]. Remarkably, the radial profiles for the valley polarization and valley coherence exhibit very different behaviour. The valley polarization, shown in Supplementary Note 3, is found to be spatially independent for excitation powers below 2 mW. This indicates that the mechanism responsible for the valley polarization enhancement in this power range is spatially homogeneous. In our scenario, this implies that the local temperature T_L varies slowly across the PL spot size. This is consistent with the absence of a clear halo-like profile for the PL intensity[31]. At higher powers, exciton-exciton interactions begin to shorten the valley lifetime[36] and, therefore, generate a spatial dependence of the emitted circular polarization which exhibits a small dip at the center above a few mW. Valley coherence, in contrast, develops a significant dip at $r = 0$ above 1 mW as shown in Fig. 4b, consistent with the strong variation of the valley
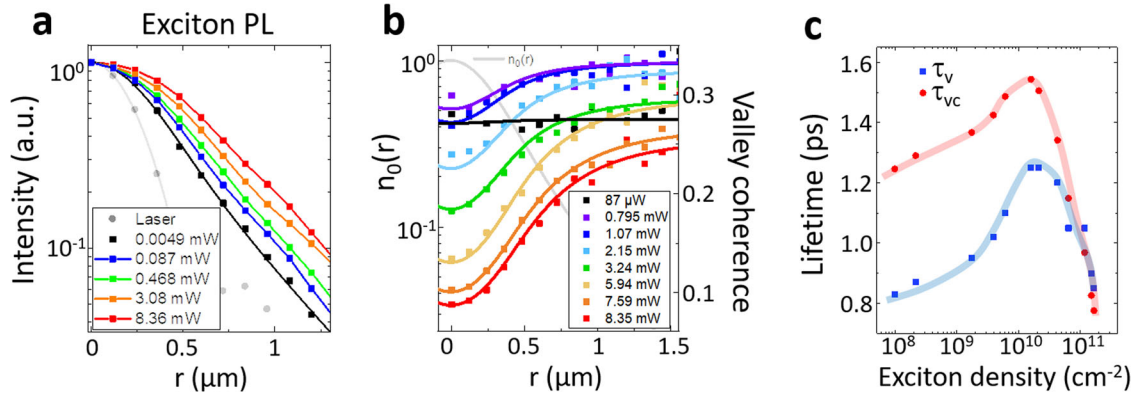
Fig. 4 Spatial dependence of valley coherence at high excitation densities T=6 K. a Normalized PL profiles for selected excitation powers. **b** Spatially resolved valley coherence for selected excitation powers. The continuous lines are obtained by fitting with Eq. (4). Also shown is the normalized concentration profile $n_0(r)$. (**c**) Extracted valley lifetime τ_v and valley coherence time τ_{vc} from the fitting of the curves shown in (**b**). The continuous liens are a guide to the eye.

dephasing time γ_v^* with exciton concentration deduced from Fig. 3c. Since γ_v^* varies much more than τ_v with the exciton density in this regime, the spatial dependence of the valley coherence reflects directly the influence of the local exciton density $n(r)$ on the pure valley dephasing time $\gamma_v^*(r)$. To test the validity of our interpretation, we have fitted the spatial dependence of the valley coherence $\mathcal{P}_L(r) = \tau_{vc}(r)/\tau$ with a simple model that considers $\tau = 5$ ps and the valley lifetime τ_v as constants and takes into account the spatial variation of the exciton density n on the valley-coherence time through Eq. (3), so that

$$\tau_{vc}(r) = \left(\frac{1}{2\tau_v} + \gamma_v^*(n(r))\right)^{-1} \quad (4)$$

Here, $n(r) = aP_{ex}n_0(r)$ where a is a free parameter of the model, P_{ex} is the excitation power and n_0 is the normalized convoluted solution of the diffusion equation which reproduces the PL profile at low power. The resulting curves (together with $n_0(r)$ for comparison) are shown as solid lines in Fig. 4b, reproducing quite well the experimental data with $a = 0.42 \times 10^{11}$ cm^{-2}mW^{-1}. The valley lifetime τ_v is treated as a free parameter for each excitation power, and the result as a function of the (spatially averaged) exciton density is shown in Fig. 4c, together with the valley coherence time τ_{vc}. Of course, these extracted lifetimes depend on the particular choice of τ that we have used, and should not be considered as precise since they are the result of a rather simple model that captures nevertheless the essential physics behind the spatial variation of the valley coherence. Below 10^{10} cm^{-2}, both lifetimes are enhanced due to the increase of τ_v with the local temperature, whereas above $n^* = 10^{10}$ cm^{-2} the exciton-exciton interactions reduce τ_v but also γ_v^*, the result being a dramatic drop of the valley coherence time τ_{vc}. Although the identification of the exact mechanism by which exciton-exciton interactions shortens the pure dephasing time γ_v^* goes beyond the scope of this work, one can consider for example a polarization-dependent exciton-exciton interaction. This leads to a precession of the valley pseudospin around the z-axis, similar to the mechanism predicted for exciton polaritons in microcavities[39,40].

CONCLUSIONS
In summary, this work brings additional elements for the understanding of the different mechanisms that may influence the dynamics of valley polarization and valley coherence in TMD monolayers. We have shown that, in addition to increasing the sample temperature or the resident carrier density, valley polarization can be enhanced by increasing the photogenerated

exciton density up to ~10^{10} cm^{-2}. Further increase of the excitation density, together with the significant increase of the local temperature, compensate (and eventually counteracts) this enhancement of valley polarization. Valley coherence is shown to be only moderately enhanced, before dropping quickly as a function of the exciton density due to a significant increase on the pure dephasing rate, demonstrating the detrimental effect of exciton-exciton interactions for the preservation of coherent superposition of valley excitons.

METHODS
Encapsulated MoS$_2$ monolayers such as the one shown in Fig. 1a, b were fabricated by mechanical exfoliation of bulk molybdenite crystals from the manufacturer's 2D semiconductors. The layers were deterministically and sequentially transferred onto an SiO$_2$ (90 nm)/Si substrate by using a transparent viscoelastic stamp[41]. A hyperspectral confocal micro-PL set-up is used to excite and detect the polarized exciton emission at cryogenic temperatures[42,43]. The samples are excited with a continuous wave (cw) solid-state laser at 633 nm (~1.96 eV), tightly focused onto a diffraction-limited spot in the sample plane. At $T = 6$ K, this laser is detuned by 23 meV from the neutral exciton transition. The Airy-disk of the laser's intensity on the sample plane can be approximated by a gaussian profile of the form e^{-r^2/σ^2}, with r the radial distance from the center of the laser spot and $\sigma \approx 0.3\,\mu$m. The polarization of both the laser and the detected PL is controlled with liquid crystal retarders and linear polarizers. The resulting PL spot is imaged onto the entrance slit of a 320 mm focal length spectrometer equipped with a 600 grooves/mm diffraction grating. For PL imaging, tunable filters were used to select the neutral exciton emission, whose spatial distribution was then imaged onto a cooled Si-CCD camera.

Reporting summary
Further information on research design is available in the Nature Research Reporting Summary linked to this article.

DATA AVAILABILITY
The datasets generated and/or analyzed during the current study are available from the corresponding author on reasonable request.

REFERENCES
1. Behnia, K. Condensed-matter physics: polarized light boosts valleytronics. *Nat. Nanotechnol.* **7**, 488 (2012).

2. Xiao, D., Liu, G.-B., Feng, W., Xu, X. & Yao, W. Coupled spin and valley physics in monolayers of MoS2 and other group-vi dichalcogenides. *Phys. Rev. Lett.* **108**, 196802 (2012).

3. Butler, S. Z. et al. Progress, challenges, and opportunities in two-dimensional materials beyond graphene. *ACS Nano* **7**, 2898 (2013).

4. Li, L. et al. Room-temperature valleytronic transistor. *Nat. Nanotechnol.* **15**, 743 (2020).

5. Li, L. et al. Electrical switching of valley polarization in monolayer semiconductors. *Phys. Rev. Mater.* **4**, 104005 (2020).

6. Huang, Z. et al. Robust room temperature valley hall effect of interlayer excitons. *Nano Lett.* **20**, 1345 (2020).

7. Ramasubramaniam, A. Large excitonic effects in monolayers of molybdenum and tungsten dichalcogenides. *Phys. Rev. B* **86**, 115409 (2012).

8. Ross, J. S. et al. Electrical control of neutral and charged excitons in a monolayer semiconductor. *Nat. Commun.* **4**, 1474 (2013).

9. Mak, K. F. et al. Tightly bound trions in monolayer MoS2. *Nat. Mater.* **12**, 207 (2013).

10. Cao, T. et al. Valley-selective circular dichroism in MoS2. *Nat. Commun.* **3**, 887 (2012).

11. Mak, K. F., He, K., Shan, J. & Heinz, T. F. Control of valley polarization in monolayer MoS2 by optical helicity. *Nat. Nanotechnol.* **7**, 494 (2012).

12. Zeng, H., Dai, J., Yao, W., Xiao, D. & Cui, X. Valley polarization in mos$_2$ monolayers by optical pumping. *Nat. Nanotechnol.* **7**, 490 (2012).

13. Sallen, G. et al. Robust optical emission polarization in MoS2 monolayers through selective valley excitation. *Phys. Rev. B* **86**, 081301 (2012).

14. Kioseoglou, G. et al. Valley polarization and intervalley scattering in monolayer MoS2. *Appl. Phys. Lett.* **101**, 221907 (2012).

15. Robert, C. et al. Exciton radiative lifetime in transition metal dichalcogenide monolayers. *Phys. Rev. B* **93**, 205423 (2016).

16. Jakubczyk, T. et al. Radiative limited dephasing and exciton dynamics in MoSe$_2$ monolayers revealed with four-wave mixing microscopy. *Nano Lett.* **16**, 5333 (2016).

17. Jones, A. M. et al. Optical generation of excitonic valley coherence in monolayer WSe$_2$. *Nat. Nanotechnol.* **8**, 634 (2013).

18. Wang, Z., Zhao, L., Mak, K. F. & Shan, J. Probing the spin-polarized electronic band structure in monolayer transition metal dichalcogenides by optical spectroscopy. *Nano Lett.* **17**, 740 (2017).

19. Cadiz, F. et al. Excitonic linewidth approaching the homogeneous limit in MoS2 based van der Waals heterostructures : accessing spin-valley dynamics. *Phys. Rev. X* **7**, 021026 (2017).

20. Wu, Y., Taniguchi, T., Watanabe, K. & Yan, J. Enhancement of exciton valley polarization in monolayer MoS2 induced by scattering. *Phys. Rev. B* **104**, L121408 (2021).

21. Barbone, M. et al. Charge-tuneable biexciton complexes in monolayer WSe$_2$. *Nat. Commun.* **9**, 3721 (2018).

22. Martin, E. W. et al. Encapsulation narrows and preserves the excitonic homogeneous linewidth of exfoliated monolayer MoSe$_2$. *Phys. Rev. Appl.* **14**, 021002 (2020).

23. Zhu, C. R. et al. Exciton valley dynamics probed by Kerr rotation in WSe$_2$ monolayers. *Phys. Rev. B* **90**, 161302 (2014).

24. Yan, T., Ye, J., Qiao, X., Tan, P. & Zhang, X. Exciton valley dynamics in monolayer WSe$_2$ probed by the two-color ultrafast Kerr rotation. *Phys. Chem. Chem. Phys.* **19**, 3176 (2017).

25. Wang, G. et al. Valley dynamics probed through charged and neutral exciton emission in monolayer WSe$_2$. *Phys. Rev. B* **90**, 075413 (2014).

26. Glazov, M. M. et al. Spin and valley dynamics of excitons in transition metal dichalcogenide monolayers. *Physica Status Solidi (b)* **252**, 2349 (2015).

27. Yu, T. & Wu, M. W. Valley depolarization due to intervalley and intravalley electron-hole exchange interactions in monolayer mos$_2$. *Phys. Rev. B* **89**, 205303 (2014).

28. M.D'yakonov & Perel, V. I. Spin relaxation of conduction electrons in non-centrosymmetric semiconductors. *Sov. Phys. Solid State* **13**, 3023 (1972).

29. Wang, Z. et al. Intravalley spin-flip relaxation dynamics in single-layer WS2. *Nano Lett.* **18**, 6882 (2018).

30. Ghazaryan, A., Hafezi, M. & Ghaemi, P. Anisotropic exciton transport in transition-metal dichalcogenides. *Phys. Rev. B* **97**, 245411 (2018).

31. Park, S. et al. Imaging Seebeck drift of excitons and trions in MoSe$_2$ monolayers. *2D Mater* **8**, 045014 (2021).

32. Cordovilla Leon, D. F., Li, Z., Jang, S. W. & Deotare, P. B. Hot exciton transpot in WSe$_2$ monolayers. *Phys. Rev. B* **100**, 241401(R) (2019).

33. Fang, H. H. et al. Control of the exciton radiative lifetime in van der Waals heterostructures. *Phys. Rev. Lett.* **123**, 067401 (2019).

34. Cadiz, F. et al. Ultra-low power threshold for laser induced changes in optical properties of 2D molybdenum dichalcogenides. *2D Mater.* **3**, 045008 (2016).

35. Oertel, S., Hubner, J. & Oestreich, M. High temperature electron spin relaxation in bulk GaAs. *Appl. Phys. Lett.* **93**, 132112 (2008).

36. Mahmood, F., Alpischshev, Z., Lee, Y., Kong, J. & Gedik, N. Observation of exciton-exciton interaction mediated valley depolarization in monolayer MoSe$_2$. *Nano Lett.* **18**, 223 (2018).

37. Kulig, M. et al. Exciton diffusion and halo effects in monolayer semiconductors. *Phys. Rev. Lett.* **120**, 207401 (2018).

38. Perea-Causin, R. et al. Exciton propagation and halo formation in two-dimensional materials. *Nano Lett.* **19**, 7317 (2019).

39. Shelykh, I., Malpuech, G., Kavokin, K. V., Kavokin, A. V. & Bigenwald, P. Spin dynamics of interacting exciton polaritons in microcavities. *Phys. Rev. B* **70**, 115301 (2004).

40. Glazov, M. M., Semina, M. A., Sherman, E. Y. & Kavokin, A. V. Spin noise of exciton polaritons in microcavities. *Phys. Rev. B* **88**, 041309(R) (2013).

41. Castellanos-Gomez, A. et al. Deterministic transfer of two-dimensional materials by all-dry viscoelastic stamping. *2D Mater.* **1**, 011002 (2014).

42. Favorskiy, I. et al. Circularly polarized luminescence microscopy for the imaging of charge and spin diffusion in semiconductors. *Rev. Sci. Instrum.* **81**, 103902 (2010).

43. Cadiz, F. et al. Exciton diffusion in WSe$_2$ monolayers embedded in a van der Waals heterostructure. *Appl. Phys. Lett.* **112**, 152106 (2018).

ACKNOWLEDGEMENTS

AUTHOR CONTRIBUTIONS

F.C. conceived and planned the experiments, and supervised the findings of this work. F.C. and S.G. carried out the experiments and data treatment. F.C. wrote the manuscript. T.T. and K.W. have provided the hBN crystals.

COMPETING INTERESTS

The authors declare no competing interests.

ADDITIONAL INFORMATION

Supplementary information The online version contains supplementary material available at https://doi.org/10.1038/s41699-022-00303-x.

Correspondence and requests for materials should be addressed to F. Cadiz.

Reprints and permission information is available at http://www.nature.com/reprints

Publisher's note Springer Nature remains neutral with regard to jurisdictional claims in published maps and institutional affiliations.